

Novel Single-Turn Coupled-Inductor with MHz-Range Operation in Triangular Current Mode for 48 to 12 V conversion

Track 6. Vehicle Electrification-related Technologies

Abstract—The next generation of automotive vehicles and datacenters requires highly compact and efficient 48 V to 12 V point-of-load converters. This paper presents a novel single-turn planar inductor geometry with four poles and dual air-gap for operation beyond 1 MHz that minimizes copper-losses from external proximity effect. An experimental prototype with 1 kW output achieves an impressive power density of 80 kW/l (1300 W/in³) and a peak efficiency of 96.3%, demonstrating the potential of the inductor structure.

Index Terms—automotive 48 V to 12 V, coupled inductor, high power density, soft-switching

I. INTRODUCTION

With a growing power demand, power distribution in both conventional and electric vehicles presents an increasing challenge. Traditionally, 12 V are used to distribute the power to all auxiliary devices which requires large cable diameters. Moving to a 48 V distribution bus reduces the cost of the wire assembly and losses [1]. As most devices are still operating at 12 V, highly compact and efficient point-of-load converters are required. This conversion stage is a critical part of distributed power architectures and its performance has a direct impact on system-level efficiency, thermal design, and overall build volume [1]. With the rise of Gallium Nitride (GaN) power devices, operating converters in the MHz-range has become feasible, significantly reducing their size [2]. Resonant converters with planar transformers are a common choice but are unsuitable when a regulated output voltage is required over a wide input voltage range. The classical buck converter is suited well for those cases but the design of compact and efficient planar inductors is challenging due to the missing possibility for interleaving, the fringing of the air-gap, and the DC-bias in the core.

In this paper, a 1 kW 2-phase coupled inductor buck converter for 48 to 12 V conversion is studied. To minimize the overall volume, a target switching-frequency range of 1 to 3 MHz was selected. Compared to previous work [3]–[7], the low operating voltage requires a very low inductance whose design becomes particularly challenging due to the large phase current of 40 A with 100 A of ripple (required to achieve soft-switching). Firstly, the effects of coupling on the electrical parameters are analyzed mathematically. Afterwards, different geometries for the single-turn inductor are optimized using a novel winding geometry and dual air-gaps. The most promising geometry based on the four-pole structure is implemented and tested in an experimental prototype.

II. COUPLED INDUCTOR BUCK CONVERTER IN TCM

a) Working principle: The topology of the two phase coupled-inductor buck converter is shown in Fig. 1. It operates like a conventional two-phase buck with both legs are switched 180° out of phase. When the leg 2 is pulled high, the current in leg 1 is also affected as shown in Fig. 2: For positive coupling, the falling slope is steepened while for negative coupling it is flattened. The converter operates at very high ripple, more than twice the phase current. The low-side switch is kept on for a short period of time after the zero-crossing of the leg current such that the current becomes negative prior to the rising edge of each leg resulting in a zero voltage switching (ZVS) turn-on of all transistors. This mode is commonly called triangular current mode (TCM) [8]. Only the small turn-off losses are observed now. If the dead-time is too long, the devices enter reverse-conduction creating additional losses. In practice, these reverse-conduction losses can be almost eliminated by properly adjusting the dead-time.

b) Impact of the Coupling Factor: The symmetrical coupled inductor consists of two identical coils that are wound in a way, that the flux of one coil links with the flux of the second coil and vice versa with both coils connected on one side. This configuration can be described mathematically using

$$\begin{bmatrix} v_a \\ v_b \end{bmatrix} = \begin{bmatrix} 1 & k \\ k & 1 \end{bmatrix} L_{\text{self}} \begin{bmatrix} \frac{di_1}{dt} \\ \frac{di_2}{dt} \end{bmatrix} \quad (1)$$

with self-inductance L_{self} and coupling-factor k . Note that k can be positive or negative. In order to provide a more intuitive understanding, the equivalent circuit in Fig. 3 (b) is introduced. Both circuits are electrically equivalent for $L_{\text{out}} = (1+k) \frac{L_{\text{self}}}{2}$ and $L_m = (1-k) \frac{L_{\text{self}}}{2}$. The voltage at the virtual central node in the transformer model is only dependent on the two leg

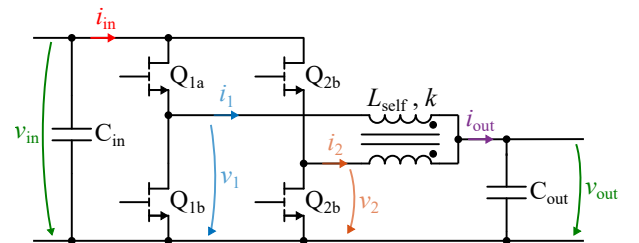


Fig. 1: Schematic of the Coupled Inductor Buck Converter.

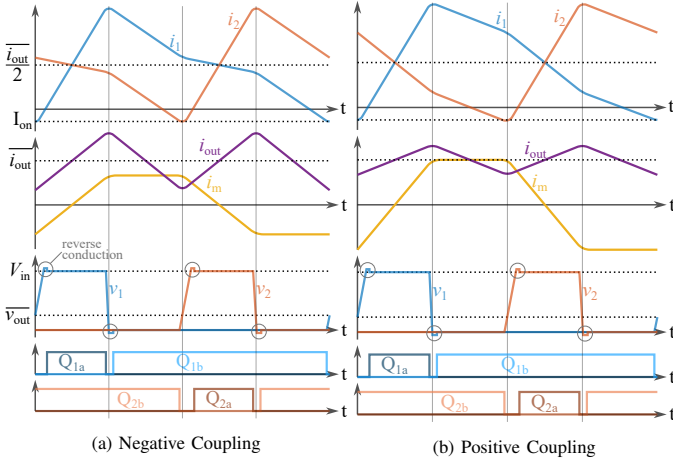


Fig. 2: Waveforms for positive and negative coupling; dead-times are exaggerated. It can be seen that the slopes are changed but the behavior in the vicinity of the switching instances is fundamentally the same.

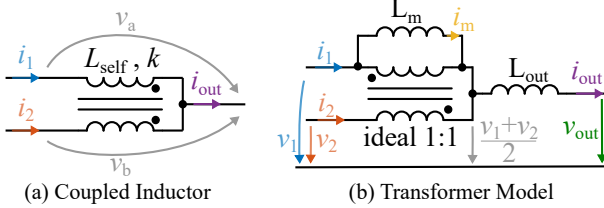


Fig. 3: The coupled inductor can be described with a self-inductance L_{self} and coupling factor k or by using an equivalent circuit consisting of an ideal 1:1 transformer with magnetizing inductance L_m and common output inductance L_{out} .

voltages v_1 and v_2 , decoupling the governing equations:

$$\begin{aligned} \frac{di_{\text{out}}}{dt} &= \frac{1}{L_{\text{out}}} \left(\frac{v_1 + v_2}{2} - v_{\text{out}} \right) \\ \frac{di_m}{dt} &= \frac{1}{L_{\text{out}}} \left(\frac{v_1 - v_2}{2} \right) \end{aligned} \quad (2)$$

$$\text{with } i_{\text{out}} = i_1 + i_2 \quad \text{and} \quad i_m = i_1 - i_2$$

From this, the differential equations for each interval can be easily calculated and equations for the important converter parameters can be derived. An effective duty cycle D_{eff} is introduced with $D_{\text{eff}} = D$ for $D \leq 0.5$ and $D_{\text{eff}} = 1 - D$ for $D > 0.5$ to create universal equations. The peak-to-peak output ripple is then given by

$$\Delta I_{\text{out}} = \frac{2V_{\text{in}}}{f_s(1+k)L_{\text{self}}} D_{\text{eff}} \left(\frac{1}{2} - D_{\text{eff}} \right). \quad (3)$$

The peak-to-peak ripple in each leg which is important for soft-switching is

$$\Delta I_{\text{leg}} = \frac{V_{\text{in}} D_{\text{eff}}}{2f_s L_{\text{self}}} \left(\frac{2}{1+k} \left(\frac{1}{2} - D_{\text{eff}} \right) + \frac{1}{1-k} \right). \quad (4)$$

I_{on} needs to be below a certain negative value $I_{\text{on,max}}$ to guarantee a sufficiently short dead time. This is fulfilled for

$$f_s < \frac{V_{\text{in}} D_{\text{eff}}}{2L_{\text{self}}(\bar{i}_{\text{out}} + 2I_{\text{on,max}})} \left(\frac{2}{1+k} \left(\frac{1}{2} - D_{\text{eff}} \right) + \frac{1}{1-k} \right). \quad (5)$$

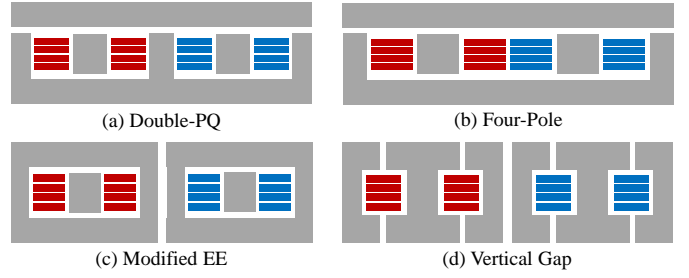


Fig. 4: Structure of the studied cores in side-view if cut through the middle. First winding in red, second winding in blue.

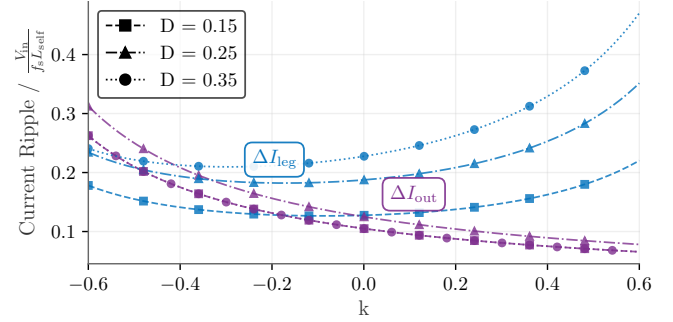


Fig. 5: Peak-to-peak leg and output current ripple in dependency of the coupling factor for different duty cycle. For $D = 0.15$ and $D = 0.35$ the output current ripple is identical so the curves overlap.

III. INDUCTOR DESIGN

a) Inductor geometry: Four different geometries, two coupled, and two uncoupled ones, were compared for this work as shown in Fig. 4. The Double-PQ structure was originally introduced by [7] and combines two EQ-cores placed next to each other. The four-pole structure is very similar but omits the central pole [6]. Both of these geometries were originally constructed with two pieces such that there is only an air-gap at the top. The dual air-gap shown in Fig. 4 is introduced in this work. The third geometry is basically an EE-Core but instead of one central gap, two gaps are used. Lastly, the vertical gap geometry proposed by [9] is investigated which can partly compensate the internal proximity effect.

All designs use a single turn with all six layers in parallel which is very different from their original designs. Designs with more than one turn were not considered because the desired inductance and coupling-factor could not be achieved in that case due to fringing.

b) Material limitations: TDK's PC200 was selected for this design as it exhibits very low loss in the range of 1 to 4 MHz. However, the performance of PC200 significantly degrades for a field strength $H_{\text{dc}} > 50$ A/m and at $H_{\text{dc}} > 100$ A/m its losses double [10]. Therefore, the inductor was designed with a maximum H_{dc} of 40 A/m to have some margin.

c) Positive vs negative coupling: Equation (3) and (4) are plotted in Fig. 5 for positive and negative coupling-factors. While a strong positive coupling decreases ΔI_{out} it increases ΔI_{leg} . Overall, positive coupling is slightly beneficial from an electrical point of view as it reduces the output ripple. The

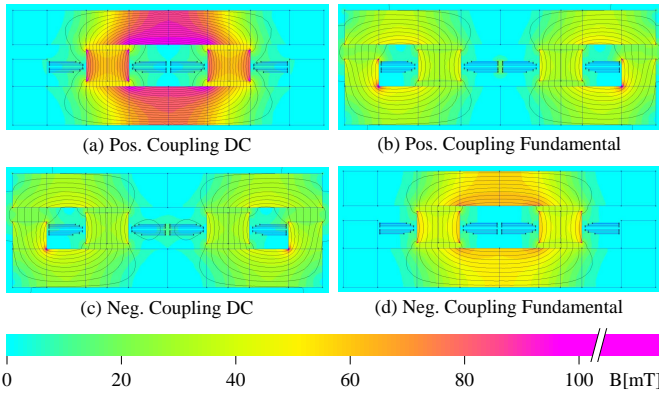


Fig. 6: Flux-Distribution for negative and positive coupling of otherwise identical designs for a DC phase current of 40 A and 100 A of ripple.

TABLE I: Comparison of the size and loss of the optimized pillar and windings for the four-pole design.

	Volume [cm ³]	Copper Loss [W]
Original design	5.8	7.0
Air-Gap on top and bottom	5.5	5.7
Air-Gap on top and bottom, curved windings	5.3	5.0

higher ΔI_{leg} requires a larger L_{self} resulting in even lower ΔI_{out} . However, there is a very notable difference in the flux distribution as shown in Fig. 6: For negative coupling, the two windings generate an opposing magnetomotive force at DC, resulting in a low flux that circulates through the outer air-gaps. For positive coupling, the two magnetomotive forces are driving a DC-flux in the same direction causing a large flux that only circulates between the two windings where the reluctance is much lower. The peak flux-density is almost three times larger for positive coupling and as the core should be designed with respect to the H_{dc} limit, this means thicker top and bottom areas would be needed. Therefore, negative coupling is selected for this application¹.

d) Simulation Process: For the simulation, the open-source 2D FEM software FEMM was used due to its high speed and easy integration with Matlab. As the core-structures are neither planar nor axisymmetric, the designs were first transformed to a planar structure. All cross-sectional areas are kept the same and the depth of the design is determined by the length of the winding.

e) Split air-gap and optimized windings: The external proximity effect caused by the air-gap plays an important role for the current distribution and consequently the losses of this high-frequency inductor. The field-strength at the top of the windings is large and almost zero at the bottom. As a result, the AC current is only flowing in the top layers. By centering the pillar vertically in the window such that there is an equal air-gap on the top and on the bottom, the field-strength is distributed much more uniformly and current flows in the top

¹Note that for lower frequency materials which are less affected by DC flux, the picture would change: Those designs would likely benefit from positive coupling as the flux-density at the fundamental is reduced.

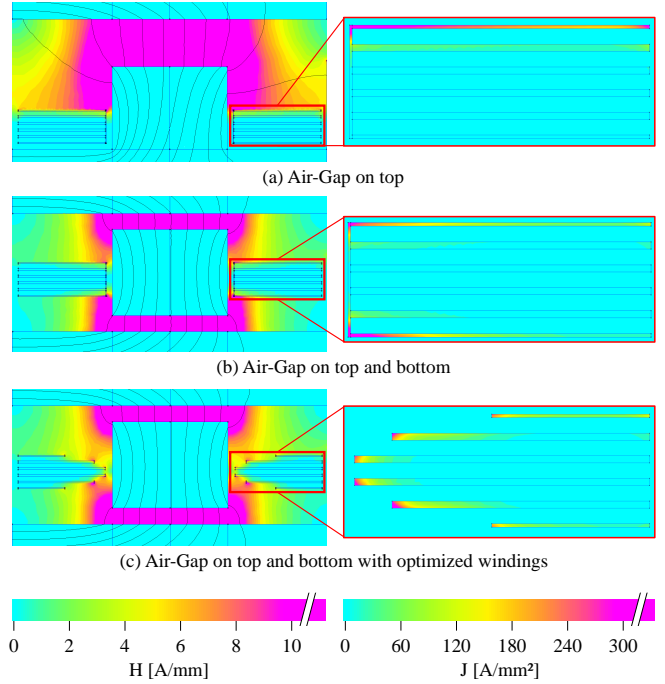


Fig. 7: Field and current distribution for different approaches. Because all layers are in parallel the current crowds in areas of large field-strength. By splitting the gap, the field gets distributed more evenly and the current distribution improves. Utilizing a smaller width for the outer layers, i.e. moving the copper away from the high-flux areas distributes the current even better.

and bottom layers. This results in a 20 % reduction in losses, which can be reduced even further by using curved windings as shown in Table I.

f) Vertical Air-Gap: The design with vertical air-gap showed a significantly lower loss compared to a traditional horizontal gap while having a much lower volume. This confirms the results from [9]. The main downside of this design is the significant external field on top and bottom of the inductor, making cooling difficult as no conductive material can be placed on top or bottom of the core.

g) Comparison of Core Structures: Table II compares the different core structures for a design with $f_s = 1.5$ MHz at $\bar{i}_{\text{out}} = 80$ A and $k = -0.3$. This coupling factor was chosen because it allows the use of small air gaps at the pillar which reduces copper losses due to the smaller external field while still not increasing ΔI_{out} too much. The cross-sectional areas were designed to result in $H_{\text{dc}} \leq 40$ A/m. All designs except the one with vertical gap use the optimized curved windings. The four-pole structure showed the lowest losses and volume and was chosen for the implementation. The inductor design is shown in Fig. 8.

IV. EXPERIMENTAL PROTOTYPE

The assembled prototype is shown in Fig. 9. The boxed volume of just 12.4 cm³ results in a power density of 80 kW/L (1300 W/in³). It's main hardware components are listed in table III. Two parallel low side transistors per phase are used as the converter operates at a low duty cycle. To minimize the stray inductance, the decoupling capacitors for the half-bridges

TABLE II: Comparison of the size and loss of the different core structures for 1.5 MHz respecting the H_{dc} limit. The Four-Pole structure shows the lowest losses and volume.

	Total Area [cm ²]	Height [cm]	Volume [cm ³]	Copper Loss [W]
Four-Pole	5.5	0.9	5.3	5.0
Double PQ	6.2	0.9	5.5	5.2
Vertical gap	8.0	0.7	5.8	5.6
UU core	8.1	1.1	8.9	6.0

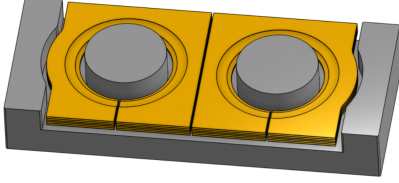


Fig. 8: Final design of the four-pole inductor; top-piece not shown.

were connected to the devices with a so-called vertical power-loop layout which uses the first inner layer as a return path [11]. In contrast to other designs, the large onboard capacitance allows the converter to operate without any additional off-board capacitance.

The converter operates over the entire range as expected. The efficiency is shown in Fig. 10 which reaches its maximum of 96.3% at around 550 W. As expected, the efficiency significantly drops for each frequency once a certain power is exceeded. This is caused by the operation in TCM: The leg-current ripple is proportional to the switching frequency and to achieve soft-switching, a certain negative current is required prior to the turn-off of the low-side switch, otherwise the voltage at the switching node will not rise fast enough to yield soft-switching. As the output current rises, the negative current rises and at some point, soft-switching is lost. To use the converter in a real application, a variable switching frequency is required. The expected resulting efficiency curve is indicated in Fig. 10.

V. CONCLUSION

Preliminary results show that the buck converter with negatively coupled, single turn inductors is capable of achieving very high power density and efficiency for 48 V to 12 V con-

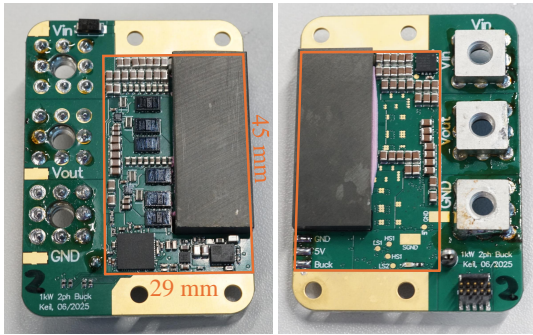


Fig. 9: Fully assembled prototype (without heatspreader). The converter area shown in orange is 45 x 29 x 9.5 mm. Outside of this area only the connectors for power and programming are placed as well as a protection diode and the programming resistors. ToDo: White Background and place match next to it.

TABLE III: Overview of the main hardware components.

Component	Part
C_{in}	44x 2.2 μ F 100 V X7R (20 μ F at 48 V)
C_{out}	16x 2.2 μ F 100 V X7R (33 μ F at 12 V)
GaN-FETs	Infineon IGC025S08S1
Gate Driver	Analog Devices LT8418
Microcontroller	Texas Instruments F280049C
Aux. Power Supply	Texas Instruments TPSM365R6
Current Sensor	Allegro ACS37220

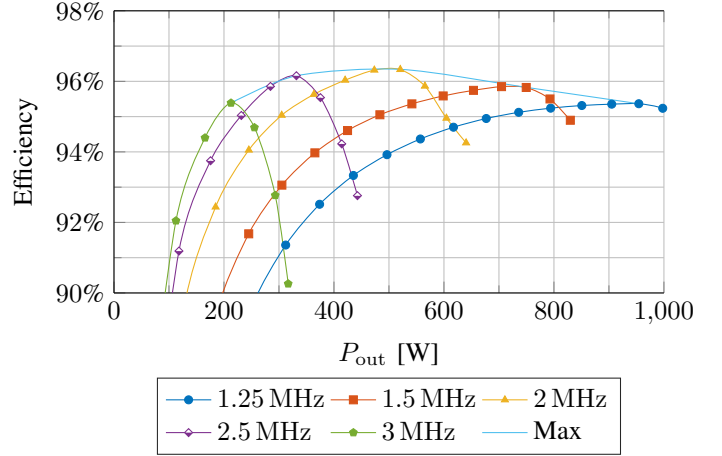


Fig. 10: Efficiency of the prototype for $V_{in} = 48$ V and $D = 0.25$.

version. Utilizing the transformer model, compact equations for the key electrical parameters were derived in dependency of the coupling factor. It was shown that positive and negative coupling are ambivalent in their electrical parameters but negative coupling creates a much lower DC flux which is important for high-frequency materials. Utilizing a dual air-gap and optimized windings, losses could be decreased significantly.

The final paper will also include a thermal analysis of the converter. The maximum achievable output power is expected to be higher than currently shown as the cooling system is not at capacity. It will also include more detailed measurements of the efficiency with a fixed conversion ratio instead of fixed duty cycle as well as efficiency in boost-mode. Furthermore, a more detailed analysis of the losses will be presented, comparing the different sources of losses in simulation with measurements from the prototype.

REFERENCES

- [1] A. K. Kumawat and A. K. Thakur, "A Comprehensive Study of Automotive 48-Volt Technology," *International Journal of Mechanical Engineering*, vol. Volume 4, Jan. 2019, publisher: SSRG International Journal. [Online]. Available: <https://www.internationaljournalssrg.org/IJME/paper-details?Id=73>
- [2] N. Weitz, S. Ehrlich, P. Freundl, J. Schültzke, and M. März, "A High Frequency Resonant Push-Pull Converter with a Single Integrated Magnetic Component," in *2023 IEEE Applied Power Electronics Conference and Exposition (APEC)*, Mar. 2023, pp. 435–440, iSSN: 2470-6647. [Online]. Available: <https://ieeexplore.ieee.org/document/10131366>

- [3] C. Nan and R. Ayyanar, "A 1 MHz bi-directional soft-switching DC-DC converter with planar coupled inductor for dual voltage automotive systems," in *2016 IEEE Applied Power Electronics Conference and Exposition (APEC)*, Mar. 2016, pp. 432–439. [Online]. Available: <https://ieeexplore.ieee.org/abstract/document/7467908>
- [4] Y. Dong, "Investigation of Multiphase Coupled-Inductor Buck Converters in Point-of-Load Applications," Jul. 2009, publisher: Virginia Tech. [Online]. Available: <http://hdl.handle.net/10919/28469>
- [5] D. Sha, Y. Zhao, and D. Zhang, "ZVS-Interleaved Synchronous Buck DC-DC Converter With a Coupled Inductor by Varying Switching Frequency and Deadtime," *IEEE Transactions on Power Electronics*, vol. 37, no. 7, pp. 8190–8198, Jul. 2022, conference Name: IEEE Transactions on Power Electronics. [Online]. Available: <https://ieeexplore.ieee.org/abstract/document/9674799>
- [6] M. Hua, J. Chen, G. Xu, and H. Wu, "Ultra-thin Coupled Inductor for a GaN-Based CRM Buck Converter," in *2021 IEEE Workshop on Wide Bandgap Power Devices and Applications in Asia (WiPDA Asia)*, Aug. 2021, pp. 138–142. [Online]. Available: <https://ieeexplore.ieee.org/document/9656036/citations#citations>
- [7] S. Wang, P. H. Pham, Q. Li, A. Nabih, and P. R. Prakash, "PCB Winding-Based Coupled Inductor for a High-Frequency DC/DC Converter with 99% Efficiency," in *2023 IEEE Applied Power Electronics Conference and Exposition (APEC)*, Mar. 2023, pp. 420–425, ISSN: 2470-6647. [Online]. Available: <https://ieeexplore.ieee.org/document/10131439>
- [8] C. Marxgut, J. Biela, and J. W. Kolar, "Interleaved Triangular Current Mode (TCM) resonant transition, single phase PFC rectifier with high efficiency and high power density," in *The 2010 International Power Electronics Conference - ECCE ASIA -*, Jun. 2010, pp. 1725–1732. [Online]. Available: <https://ieeexplore.ieee.org/document/5542048>
- [9] J. Schäfer, D. Bortis, and J. W. Kolar, "Novel Highly Efficient/Compact Automotive PCB Winding Inductors Based on the Compensating Air-Gap Fringing Field Concept," *IEEE Transactions on Power Electronics*, vol. 35, no. 9, pp. 9617–9631, Sep. 2020, conference Name: IEEE Transactions on Power Electronics. [Online]. Available: <https://ieeexplore.ieee.org/document/8968357>
- [10] TDK, "High-Frequency, Low-Loss Ferrite Material PC200." [Online]. Available: https://product.tdk.com/de/techlibrary/productoverview/ferrite_pc200.html
- [11] D. Reusch and J. Strydom, "Understanding the Effect of PCB Layout on Circuit Performance in a High-Frequency Gallium-Nitride-Based Point of Load Converter," *IEEE Transactions on Power Electronics*, vol. 29, no. 4, pp. 2008–2015, Apr. 2014. [Online]. Available: <https://ieeexplore.ieee.org/document/6531683>